

AN *XMM-Newton* STUDY OF THE CORONAE OF σ^2 CORONAE BOREALIS

JIN A. SUH AND MARC AUDARD¹

Columbia Astrophysics Laboratory, Mail code 5247, 550 West 120th Street, New York, NY 10027

AND

MANUEL GÜDEL

Paul Scherrer Institut, 5232 Villigen PSI, Switzerland

AND

FREDERIK B. S. PAERELS

Columbia Astrophysics Laboratory, Mail code 5247, 550 West 120th Street, New York, NY 10027

To appear in the Astrophysical Journal

ABSTRACT

We present results of *XMM-Newton* Guaranteed Time observations of the RS CVn binary σ^2 Coronae Borealis. The spectra obtained with the Reflection Grating Spectrometers and the European Photon Imaging Camera MOS2 were simultaneously fitted with collisional ionization equilibrium plasma models to determine coronal abundances of various elements. Contrary to the solar first ionization potential (FIP) effect in which elements with a low FIP are overabundant in the corona compared to the solar photosphere, and contrary to the “inverse” FIP effect observed in several active RS CVn binaries, coronal abundance ratios in σ^2 CrB show a complex pattern as supported by similar findings in the *Chandra* HETGS analysis of σ^2 CrB with a different methodology (Osten et al. 2003). Low-FIP elements (< 10 eV) have their abundance ratios relative to Fe consistent with the solar photospheric ratios, whereas high-FIP elements have their abundance ratios increase with increasing FIP. We find that the coronal Fe abundance is consistent with the stellar photospheric value, indicating that there is no metal depletion in σ^2 CrB. However, we obtain a higher Fe absolute abundance than in Osten et al. (2003). Except for Ar and S, our absolute abundances are about 1.5 times larger than those reported by Osten et al. (2003). However, a comparison of their model with our *XMM-Newton* data (and vice versa) shows that both models work adequately in general. We find, therefore, no preference for one methodology over the other to derive coronal abundances. Despite the systematic discrepancy in absolute abundances, our abundance ratios are very close to those obtained by Osten et al. (2003). Finally, we confirm the measurement of a low density in O VII ($< 4 \times 10^{10}$ cm⁻³), but could not confirm the higher densities measured in spectral lines formed at higher temperatures derived by other studies of σ^2 CrB due to the lower spectral resolution of the *XMM-Newton* grating spectrometers.

Subject headings: stars: activity — stars: coronae — stars: individual (σ^2 CrB) — stars: flare — stars: late-type — X-rays: stars

1. INTRODUCTION

Studies of stellar coronae with X-ray missions such as *XMM-Newton* and *Chandra* have shown peculiar abundance patterns when compared to the coronal composition of the Sun. In the latter, elements with a first ionization potential (FIP) below about 10 eV appear, on average, overabundant compared to the high-FIP elements by a factor of a few (e.g., Meyer 1985). In addition, high-FIP elements are of solar photospheric composition (e.g., Feldman 1992; Laming, Drake, & Widing 1995). This abundance pattern is known as the “solar FIP effect”. Previous studies of stellar coronae with lower-resolution detectors than available onboard with *XMM-Newton* and *Chandra* and in the extreme ultraviolet range have shown a general depletion of the metal abundance (e.g., Antunes et al. 1994; White et al. 1994; Schmitt et al. 1996), and evidence for a solar-like FIP effect in some stars (Drake et al. 1997; Laming & Drake 1999) or its absence in others (Drake et al. 1995).

XMM-Newton and *Chandra* have reached unprecedented spectral resolution and sensitivity in the X-ray regime thanks

to their grating spectrometers. This led to the discovery of an “inverse” FIP effect in HR 1099 (Brinkman et al. 2001; Drake et al. 2001), in which low-FIP elements are underabundant compared to the high-FIP elements. Other studies have strengthened the evidence for the presence of an inverse FIP effect in magnetically active stars (e.g., Audard et al. 2001a; Güdel et al. 2001a,b; Huenemoerder et al. 2001, 2003; Audard et al. 2003; van den Besselaar et al. 2003; Raassen et al. 2003; Osten et al. 2003; Sanz-Forcada et al. 2003a), but have also shown that intermediately active stars show no strong correlation with the FIP (Audard et al. 2001b), and less active stars show a solar-like FIP effect (Güdel et al. 2002; Telleschi et al. 2005). A transition from the inverse to the solar-like FIP effect thus seems to occur with decreasing magnetic activity (Güdel et al. 2002; Audard et al. 2003). However, the inactive F star Procyon does not show any correlation between its coronal abundances and the elemental FIP (Drake et al. 1997; Raassen et al. 2002), although its cool corona (1–2 MK) should display a strong solar-like FIP effect in the transitional picture. Sanz-Forcada et al. (2004) argued that the comparison of coronal abundances to solar photospheric abundances instead of stellar photospheric abundances (which are often unknown or uncertain in the literature) could be misleading as it could falsely mimic inverse or

Electronic address: jas2010@columbia.edu, audard@astro.columbia.edu

¹ contact author

Electronic address: guedel@astro.phys.ethz.ch

Electronic address: frits@astro.columbia.edu

solar-like FIP effects in stars. On the other hand, the photospheric composition of the solar analogs in the study of Telleschi et al. (2005) is known to be similar to the Sun's; therefore, it appears that coronal abundance anomalies occur, at least in their sample.

Several theoretical studies have produced models to explain the solar FIP effect (see reviews by Héroux 1995, 1998, also Arge et al. 1998; Schwadron et al. 1999; McKenzie 2000). In the stellar context, Güdel et al. (2002) suggested that the non-thermal electrons observed in the radio could explain the inverse FIP effect in active stars, and possibly the FIP effect in inactive stars. Recently, Laming (2004) proposed a model that unifies the FIP and inverse FIP effects by exploring the effects on the upper chromospheric plasma of the wave ponderomotive forces. Laming (2004) suggested that the observed solar FIP effect could be turned into an inverse FIP effect after fine tuning model parameters. Further theoretical works are needed to address the wide range of FIP-dependent coronal abundances in the Sun and stars. In the mean time, we need to increase the sample of stars and to study their coronal abundances to understand the mechanism at the origin of the element fractionation in the Sun, and in stars. In this paper, we present the *XMM-Newton* study of the RS CVn binary σ^2 Coronae Borealis which is composed of two solar analogs as well, albeit spun up by tidal forces.

2. THE RS CVn BINARY σ^2 CORONAE BOREALIS

σ^2 CrB (HD 146361; TZ CrB) is an active RS CVn binary system at a distance of 21.7 pc (Perryman et al. 1997) whose components have spectral types of F9 V and G0 V (Strassmeier & Rice 2003). σ^2 CrB is a component of a visual binary with an orbital period of 1000 years, with the other component (σ^1 CrB) at a separation of $6.6''$. No eclipse takes place in σ^2 CrB, due to the low inclination angle of 28° (Bakos 1984), and the orbit has a period of $P = 1.14$ days (e.g., Drake et al. 1989). Strassmeier & Rice (2003) reported a 0.017 d difference between the rotation and orbital periods and interpreted it as differential rotation of the surface. The masses and radii of the components are close to solar, i.e., $M \sim 1.1M_\odot$ and $R \sim 1.2R_\odot$ (Barden 1985; Drake et al. 1989). A detailed list of the physical parameters of σ^2 CrB can be found in Strassmeier et al. (1993) and Strassmeier & Rice (2003).

The binary σ^2 CrB has been observed extensively from radio to X-rays (see Osten et al. 2000, and references therein). In the X-ray and EUV regimes, several studies have investigated the properties of the coronae of σ^2 CrB (Agrawal et al. 1981, 1985, 1986; van den Oord et al. 1988; Pasquini et al. 1989; Stern et al. 1992; Osten et al. 2000). Recently, Osten et al. (2003) presented the *Chandra* spectrum of σ^2 CrB obtained with the High-Energy Transmission Grating Spectrometer (HETGS) as part of a coordinated observing campaign in the radio, EUV, and X-ray regimes. They found a bimodal emission measure distribution with peaks at 6–8 MK and 30 MK. The Fe abundance was found to be depleted as frequently seen in bright RS CVn binaries (Audard et al. 2003), whereas Ne/Fe and Ar/Fe abundance ratios were above solar ratios. Although these ratios are indicative of an inverse FIP effect in σ^2 CrB, other elements did not show a specific correlation with the FIP. In particular, the low-FIP (6 eV) element Al was overabundant with respect to Fe. With our analysis of the *XMM-Newton* spectra, we aim to compare derived abundances with those of Osten et al. (2003). We will discuss the coronal abundances of σ^2 CrB in the context of the FIP

and inverse FIP effects in the Sun and stars.

3. OBSERVATIONS AND DATA REDUCTION

The observations of σ^2 CrB were performed by *XMM-Newton* (Jansen et al. 2001) and were spread over three epochs: 2001 August 29 (hereafter “101”), 2001 August 31 (“201”), and 2002 February 22/23 (“301”). The first observation lasted for approximately 7 ks and was interrupted by solar flare activity, therefore we will not discuss this data set further (except as a light curve in Fig. 1). Solar activity was again high for the two remaining epochs; nevertheless, we obtained spectra with sufficient quality. We provide a log of these observations in Table 1.

All data were reduced with the *XMM-Newton* Science Analysis System (SAS) 5.4.1 and the calibration files of June 2003 using standard procedures (e.g., Audard et al. 2003). The European Photon Imaging Camera (EPIC; Turner et al. 2001) MOS2 data (in SMALL WINDOW mode) were slightly piled-up, and therefore we excised the center of the point-spread function (PSF) to avoid this problem (e.g., Lumb et al. 2000). A background template was obtained from a region on an outer EPIC MOS2 CCD. Its exposure was corrected for vignetting since we assumed here that the dominant X-ray background was due to the cosmic X-ray background (i.e., the instrumental and particle backgrounds, which are not vignettted, were negligible). The EPIC MOS1 data (in TIMING mode) were not used due to the small window size which prevented us from defining an appropriate background in this mode. The EPIC pn data were taken in TIMING mode as well and will also not be discussed here.

Despite the high solar activity at the end of each observation (Fig. 1), we used the complete Reflection Grating Spectrometer (RGS; den Herder et al. 2001) data, since a comparison with the “cleaned” data (selecting periods with low solar activity) showed that they were similar. However, we preferred to use the cleaned EPIC spectra since they showed no significant contamination at high energies compared to the full-exposure spectra. We show the selected good time intervals (GTIs) in Fig. 1. Thanks to the low count rate variability of σ^2 CrB during the *XMM-Newton* observations, the different treatments of GTIs between the EPIC and the RGS data had negligible impact.

In our EPIC images, there was no evidence for X-rays from the visual binary component σ^1 CrB. Its X-ray emission could in principle be separated ($6.6''$) if it was bright enough (indeed, both Castor AB low-mass components were detected with *XMM-Newton* EPIC MOS for a separation of $3.9''$; Güdel et al. 2001b). It suggests that the X-ray luminosity of σ^1 CrB is much fainter than that of σ^2 CrB. The *Chandra* zeroth order image confirms the faintness the component (R. Osten 2003, priv. comm.). Therefore, no significant contamination by σ^1 CrB is expected in the EPIC and RGS data of σ^2 CrB.

4. DATA ANALYSIS

The reduced RGS and EPIC MOS2 spectra were fitted simultaneously using collisional ionization equilibrium (CIE) plasma models with variable elemental abundances and temperatures. A free constant multiplicative model was allowed to deal with cross-calibration normalization effects between the RGS and the EPIC spectra. We used XSPEC (Arnaud 1996) v11.2.0 software with APEC (Smith et al. 2001) code v1.3.0 that contains line and continuum emissivities. We used the Grevesse & Sauval (1998) set of solar photospheric abun-

dances. Such a set was also used by Osten et al. (2003) thus allowing a direct comparison between their and our results.

We used a multi- T approach with free temperatures and emission measures (EMs), and variable abundances (C, N, O, Ne, Mg, Si, S, Ar, Ca, Fe). We added a photoelectric absorption component using Wisconsin cross-sections of Morrison & McCammon (1983) but left the value of the column density fixed at $2 \times 10^{18} \text{ cm}^{-2}$ (Osten et al. 2000) since the *XMM-Newton* data are not sensitive to such a low value. Sanz-Forcada et al. (2003b) suggest a value of $2.5 \times 10^{18} \text{ cm}^{-2}$, but the difference is negligible. We fixed the abundance of Ni to be equal to the abundance of Fe.

Furthermore, we used a similar approach as Audard et al. (2003). Several wavelength ranges in the spectra were discarded since they include low- Z L-shell transitions which are insufficiently described in current atomic databases (Audard et al. 2001b, 2003; Lepson et al. 2003). With this procedure, we have derived the element abundances from the more reliable emission lines of low- Z K-shell ions. The full list of excluded wavelength ranges is given in Table 2.

Figures 2a-2b show the EPIC MOS2 and RGS spectra overlaid with a best fit model using a 4-temperature CIE model. The EPIC MOS2 data at wavelengths shorter than 18 \AA were used to model the high-energy tail of the X-ray spectrum and the emission lines inaccessible to the RGS; significant overlap with the RGS ($8-18 \text{ \AA}$) was kept to make sure the high- T component is well linked to the lower- T components which mainly produce emission lines in the RGS band. The hot Fe $K\alpha$ complex at 6.7 keV (weak in the EPIC MOS2 data but clearly detected in the EPIC pn data not shown here) indicates the presence of hot plasma whereas the O VII triplet reveals cool plasma. We list the best-fit parameters of 4- T CIE models for the 201 and 301 observations in Table 3. We also list the abundances reported by Osten et al. (2003) for the *Chandra* observation of σ^2 CrB.

5. DISCUSSION

5.1. Coronal Abundances

We derived absolute abundances (i.e., abundances relative to H) with respect to the solar photospheric abundances given by Grevesse & Sauval (1998). However, abundance ratios, e.g., relative to Fe, have been found to be more robust (e.g., Audard et al. 2004; Telleschi et al. 2005). Therefore we give abundance ratios to Fe in Table 3. Figure 3 shows the abundance ratios as a function of the FIP using the solar photospheric set of Grevesse & Sauval (1998). We plot the abundance ratios obtained for the 301 observation shifted by $+0.2 \text{ eV}$ for clarity. The figure shows two regimes: below 10 eV , low-FIP elements have about the same abundances and are close to the solar photospheric values. Above 10 eV , the abundance ratios increase with increasing FIP, as observed in several other RS CVn binaries (Audard et al. 2003). Figure 11 of Osten et al. (2003) shows a similar pattern, although these authors preferred to interpret it as an absence of FIP-dependent pattern.

Figure 4 shows a comparison of coronal abundances obtained in the best fits to the *XMM-Newton* 201 and 301 observations, and extends it to a comparison of the abundances obtained by Osten et al. (2003). It shows that abundance ratios are very similar for the three sets. On the other hand, the absolute abundances are systematically higher in our fits than those by Osten et al. (2003) by a factor of about 1.5. Although two different observations (e.g., at two different epochs) could, in

principle, yield different abundances because the dominant X-ray emitting regions are not the same and the observed, average, coronal composition could be different, it is far more probable that different analysis techniques could lead to different best-fit abundances (e.g., Audard et al. 2004). Furthermore, the spectral inversion problem being an ill-posed problem, small statistical variations can lead to discrepant results via the DEM inversion (Craig & Brown 1976a,b). It is, therefore, difficult to estimate which set of abundances is preferred. On the other hand, it is worthwhile to stress the robustness of abundance ratios which show (whatever the technique and the data set) that a complex FIP-dependent abundance pattern is present in σ^2 CrB's corona.

The use of a solar photospheric set of abundances to compare with stellar coronal abundances is naturally problematic, since stars can have a photospheric composition at variance from the Sun's. Magnetically active stars are difficult objects to derive accurate surface abundances in view of their rapid rotation and surface spots. Strassmeier & Rice (2003) have, however, obtained estimates of the photospheric abundances of the low-FIP elements Fe and Ca, $A_{\text{Fe}} = 7.30$ and $A_{\text{Ca}} = 6.07$ (with the usual $A_{\text{H}} = 12$ notation; they estimate an uncertainty of ~ 0.1 dex). Comparing with the solar values from Grevesse & Sauval (1998) ($A_{\text{Fe}} = 7.50$ and $A_{\text{Ca}} = 6.36$), σ^2 CrB's photosphere appears depleted with $[\text{Fe}/\text{H}] = -0.20$ and $[\text{Ca}/\text{H}] = -0.29$. Our spectral fits obtain $[\text{Fe}/\text{H}] \sim -0.15$ which is consistent with the stellar photospheric value. In contrast, Osten et al. (2003) obtain a slightly depleted coronal Fe abundance. It seems safe to conclude that the coronal Fe abundance in σ^2 CrB is close to the photospheric value, in contrast to the solar case where the coronal Fe abundance is enhanced by a factor of a few. This situation is also different from that in several magnetically active stars that show a similar U-shape abundance pattern but a net Fe depletion in their corona (e.g., Güdel et al. 2001a; Sanz-Forcada et al. 2003a; Telleschi et al. 2005). It is difficult to discuss the case of Ca since we derived large uncertainties and Osten et al. (2003) did not obtain a Ca abundance. Nevertheless, a scenario appears to emerge in which low-FIP elements are depleted in very active stars that show an inverse FIP effect. The abundances of the lowest-FIP elements in intermediately active stars rise up to be quasi-photospheric while the intermediate-FIP elements still have their abundances depleted, thus the abundance pattern shows a U shape. Finally, in the less active stars, low-FIP elements have their abundances further increased to become superphotospheric and intermediate-FIP elements have their abundances quasi-photospheric. Such stars show an abundance pattern similar to the solar FIP effect.

5.2. A Comparison with the Osten et al. Model

Our methodological approach to the *XMM-Newton* data (i.e., multi- T components) differs significantly from the approach by Osten et al. (2003) (i.e., separate treatment of continuum and lines, reconstruction of a differential emission measure [DEM] distribution based on extracted Fe line fluxes). We focus this section on comparing their model with ours. Specifically, we test whether their *Chandra* model can provide an adequate fit to our *XMM-Newton* data, and vice versa. Some caveats should be mentioned: i) Osten et al. (2003) use the APEC 1.10 version whereas we use the more recent APEC 1.3 version²; ii) σ^2 CrB's X-ray luminosity

² <http://cxc.harvard.edu/atomdb/index.html> for a detailed comparison.

was 1.39 times higher during the *XMM-Newton* observation ($L_X = 3.8 \times 10^{30}$ erg s $^{-1}$) than during the *Chandra* observation ($L_X = 2.7 \times 10^{30}$ erg s $^{-1}$). In our comparison, we will take this correction factor into account. However, it remains unclear whether this factor should be applied to all temperature components or only part of them. iii) It is possible that real changes in the X-ray spectrum (e.g., due to EM or abundance variations) occurred between the two observations. We will assume in this study that this was not the case.

We have used Osten et al.'s quiescent DEM (realization #2) together with the quiescent abundances reported in their Table 5 (we set the C and Ca abundances equal to the Fe abundance, and we set Ni=0.1 times solar photospheric, as described by Osten et al. 2003). However, after iterations with Dr. Osten, we discovered that their quiescent DEM (as shown in their Fig. 10a) is accurate from $\log T(K) = 6.0$ to 7.4 for the continuum and that the last point at $\log T(K) = 7.5$ was used only for the emission lines. However, this temperature bin essentially contributed a few tens of percent to the flux in the Fe K α complex. This oversight plays no significant role for our comparison exercise with the *XMM-Newton* data. Thus, in practice, we constructed in XSPEC a multi- T model with 15 components at temperatures at $\log T(K) = 6.0$ to 7.4 with intervals of $\Delta \log T = 0.1$ dex. We used Osten et al.'s DEM values, multiplied them by the original DEM bin width ($\Delta \log T = 0.1$ dex) to obtain the total EM for each temperature component, and further divided by 2 since Osten et al. (2003) accounted for the fact that half the radiation is absorbed by the star.

We have then convolved the model of Osten et al. (2003) in XSPEC³ (using our RGS RMF file); we have also convolved our *XMM-Newton* EPIC MOS2 (301) model through the ACIS-S/HETGS first-order RMF/ARF provided by Dr. Osten⁴. Figures 5a-5c compare the *XMM-Newton* RGS data overlaid with Osten et al.'s *Chandra* model, whereas Figures 6a-6c show the *Chandra* HETGS data (provided by Dr. Osten) overlaid with the *XMM-Newton* model.

We find surprisingly good agreement, despite different absolute abundances. There are, however, some discrepancies. In Fig 5b, the Fe XVII $\lambda 15$ Å line is overestimated compared to the *XMM-Newton* data. But this is no different from the analysis of Osten et al. (2003) which overestimated the *Chandra* Fe XVII line flux as well (see their Fig. 10a, center panel). In addition, the Osten et al. model overestimates the RGS continuum level by about 40% at wavelengths longer than 25 Å (Fig. 5c). A few possible explanations can be put forward: i) the *Chandra* HETGS wavelength range ends around 25 Å, therefore the Osten et al. model had no possibility to accurately take into account the flux beyond this instrumental limit. Sako et al. (2003) reported a similar situation in which the model of Lee et al. (2001), based on HETGS data, could reproduce the general properties of the RGS spectrum of MCG -6-30-15 below 23 Å, but it overestimated the flux for $\lambda > 25$ Å; ii) calibration problems at long wavelengths are possible; however, the 40% overestimate is larger than

the current calibration knowledge; iii) it was inadequate to multiply the EMs of Osten et al.'s model by a constant value of 1.39 to account for the X-ray luminosity difference of σ^2 CrB between the *Chandra* and *XMM-Newton* observations. It is possible that the variation is due to some part of the DEM only (e.g., at high temperatures). However, the long-wavelength continuum level is essentially determined by the high-temperature components (which describe the short and mid-wavelength ranges accurately), and, therefore we find this possibility less probable. Instead we propose that the lack of spectral coverage in the range 25–40 Å by *Chandra* HETGS slightly biased the EMD of Osten et al. (2003) to overestimate the long-wavelength flux. We note that, although Osten et al. (2003) used *EUVE* line fluxes to determine their DEM, these authors did not make use of the continuum level in the *EUVE* wavelength range (which is about 5 times lower than the continuum level at 30 Å).

Our *XMM-Newton* model (whose EMs were divided by 1.39) shows generally excellent agreement with the *Chandra* data (Fig. 6a-6c). However, the flux in the Ar XVII triplet near 4 Å was underestimated; it suggests that Ar abundances obtained from simultaneous EPIC+RGS fits might be underestimated generally. The Osten et al. model, however, predicts L-shell fluxes of Ar and S lines at long wavelengths which are consistent with the RGS data (Fig. 5c), despite the long-standing problem of the lack of atomic data of L-shell lines of low- Z elements or their inaccuracy in current atomic databases (Audard et al. 2001b; Raassen et al. 2002; Lepson et al. 2003).

With a few exceptions, we find, therefore, excellent agreement among different models derived with different techniques from different data sets, but which show very similar abundance ratios but different absolute abundances. This exercise casts some doubt on the preference of one method over the other to determine coronal abundances, and it demonstrates that the determination of true absolute abundances remains a challenge.⁵ Other studies support this interpretation. For example, Audard et al. (2004) studied the bright FK Com-type giant YY Men using different methods and found that, for a given data set (either *Chandra* or *XMM-Newton*), slight differences in absolute abundances were derived. However, they found excellent agreement for the abundance ratios relative to Fe. In parallel, Telleschi et al. (2005) studied the *XMM-Newton* data of a sample of solar analogs with different methods as well. They also observed the robustness of abundance ratios and demonstrated the presence of a transition from a solar-like FIP effect in inactive stars to an inverse FIP effect in active stars. Garcia-Alvarez et al. (2005) used one method but different sets of emission lines to derive the coronal abundances in AB Dor (and V471 Tau) and found similar abundances. They further compared their results with those in earlier studies and found good agreement in the general trend, albeit with some significant differences. Thus, in brief, despite the use of various methodologies, abundance patterns as a function of the FIP appear robust and look dependent on the magnetic activity level. However, it remains challenging i)

³ Osten et al. (2003) used the composite trapezoidal rule to integrate the line and continuum flux at a specific wavelength. The composite trapezoidal rule helps to calculate the integral of a function $f(x)$ over an interval $[a, b]$ subdivided into N subintervals $[x_i, x_{i+1}]$ of widths $h = (b-a)/N$ (thus $x_i = a + i \times h$ for $i = 0, 1, \dots, N$). The integral is then equal to $h \times (f(a) + f(b))/2 + h \times \sum_{i=1}^{N-1} f(x_i)$. Thus, we used half the DEM values at $\log T(K) = 6.0$ and 7.4 in XSPEC.

⁴ We have checked that our 15- T model based on Osten et al.'s model was correct by convolving it through the same *Chandra* response matrix files and comparing it with their synthesized model provided by Dr. Osten.

⁵ Although not shown in this paper, we note that setting the absolute Fe abundance to solar photospheric and using the same abundance ratios as provided by Osten et al. (2003), it is impossible to obtain a reasonably good fit of the *Chandra* data by simply multiplying the EMs by a constant factor. If the model is adjusted to match the continuum level, the Fe line fluxes are indeed systematically overestimated. It again reinforces the result that Fe is underabundant in σ^2 CrB's corona compared to the solar photospheric Fe abundance.

to constrain absolute abundances, and ii) to compare coronal abundances to their photospheric counterparts.

5.3. Electron Density

High-resolution X-ray spectra observed with *XMM-Newton* and *Chandra* allow us to determine electron densities from line ratios of He-like ions. The ratio R of the flux in the forbidden (f) line to the flux in the intercombination (i) line is indeed density-sensitive. In particular, the O VII triplet is most useful in measuring coronal densities of the order of 10^{10} cm^{-3} , and is relatively blend-free (in contrast to Ne IX), and well-resolved (in contrast to, e.g., Mg XI and Si XIII for the RGS). We have obtained line fluxes for the O VII triplet using delta functions convolved through the instrumental response. We list them in Table 4 together with 68% confidence ranges ($\Delta\chi^2 = 1$). The R ratio is equal to 2.81 ± 0.77 , corresponding to an upper limit to the electron density of $4 \times 10^{10} \text{ cm}^{-3}$ (Porquet et al. 2001), assuming a photoexcitation contribution by the radiation field with $T_{\text{eff}} \sim 6,000 \text{ K}$.

Osten et al. (2003) and Testa et al. (2004) reported for O VII an electron density of $\sim 2 \times 10^{10} \text{ cm}^{-3}$, i.e., consistent with ours. These authors and Sanz-Forcada et al. (2003b) quote (higher) electron densities from other He-like triplets and Fe lines (in the EUV range) which we cannot confirm due to the poorer spectral resolution of the RGS (or the lack of wavelength coverage). Unfortunately, the N VI triplet is too faint to measure any line flux.

5.4. Opacity

Our CIE models assume an optically thin plasma, so it is necessary to verify that opacity effects play a negligible role. We examined the ratio of the Fe XVII spectral lines at 15.01 \AA and at 15.26 \AA , since this ratio is sensitive to opacity effects (the 15.01 \AA line has a large oscillator strength). The measured Fe XVII fluxes are shown in Table 4.

Until recently, theoretical values for the ratio used to range from 3.0 to 4.7 (Bhatia & Doschek 1992), significantly different from laboratory measurements which suggest a range from 2.8 to 3.2 (Brown et al. 1998; Laming et al. 2000; Brown et al. 2001). However, recent theoretical work has brought the theoretical ratio closer to the laboratory ratio (Chen & Pradhan 2002; Chen et al. 2003; Fournier & Hansen 2005). We obtain a flux ratio in σ^2 CrB of 3.02 ± 0.15 , i.e., consistent with the ratios derived by Osten et al. (2003) (3.01 ± 0.26 with HEG and 2.94 ± 0.15 with MEG). Ness et al. (2003) derived a slightly lower ratio (2.56 ± 0.13), probably because of a different treatment of the continuum. Nevertheless, they also concluded that this value was close to the ratio obtained in laboratory measurements. Thus, the line ratio indicates that there are no significant opacity effects in the coronae of σ^2 CrB.

6. SUMMARY AND CONCLUSIONS

We have presented a study of the *XMM-Newton* observations of the binary σ^2 CrB. No large flare was detected during the observations. We focused our analysis on the determination of the coronal abundances by means of a multi- T approach. Although such models do not give an accurate representation of the coronal DEM, they suffice to obtain good measurements of coronal abundances and abundance ratios in particular (e.g., Audard et al. 2004; Telleschi et al. 2005). We have, furthermore, compared our resulting abundances with those of Osten et al. (2003) who published the

Chandra data of σ^2 CrB. We find very good agreement between their abundance ratios (relative to the Fe abundance) and ours, but find a systematic difference in the absolute abundances. Upon checking whether their model could fit our *XMM-Newton* data, we have obtained an excellent agreement (after correcting the published DEM, see Section 5.2).

At wavelengths longer than 25 \AA , their model overestimates the continuum level. We argue that their model, based on HETGS data below this wavelength, did not constrain their DEM well enough to account for the longer wavelength range. Our *XMM-Newton* best-fit model also reproduces the *Chandra* HETGS spectra remarkably well. Thus, abundance ratios are found to be robust, whereas the discrepancy in absolute abundances found between our model and Osten et al.'s model probably stems from the different methodologies. Similar results have been found elsewhere (Audard et al. 2004; Telleschi et al. 2005; Garcia-Alvarez et al. 2005). Nevertheless the presence of abundance patterns as a function of the FIP seems reliable.

The abundance ratios relative to the coronal Fe abundance showed a correlation with the FIP, but such a correlation was neither similar to the inverse FIP effect observed in very active binaries (e.g. Audard et al. 2003) nor to the solar-like FIP effect observed in less active stars (e.g. Telleschi et al. 2005). The abundance ratios of low-FIP elements ($< 10 \text{ eV}$) with respect to Fe are similar to the solar photospheric abundance ratios; for intermediate-FIP elements, they are however considerably lower but increase with increasing FIP. Such an abundance pattern has already been observed in other magnetically active stars (Güdel et al. 2001a; Sanz-Forcada et al. 2003a; Huenemoerder et al. 2003). However, Garcia-Alvarez et al. (2005) found the abundances of the very low-FIP elements (Al, Ca, Na) in AB Dor to be similar to, or lower than, those of low FIP (Mg, Si, Fe), in contrast to Sanz-Forcada et al.'s results. It is possible that these patterns are real, but we emphasize that coronal abundances are often compared to the solar photospheric composition due to the lack of available or reliable measurements in magnetically active, fast-rotating stars. In the case of σ^2 CrB, the Fe and Ca photospheric abundances of the σ^2 CrB binary were available (Strassmeier & Rice 2003) and suggested that the low Fe abundance in σ^2 CrB's coronae was in fact consistent with the photospheric value.

Finally, we obtained an upper limit of the coronal density based on the O VII triplet ($n_e < 4 \times 10^{10} \text{ cm}^{-3}$) which is consistent with other measurements in σ^2 CrB (Osten et al. 2003; Testa et al. 2004). Osten et al. (2003), Sanz-Forcada et al. (2003b), and Testa et al. (2004) found higher densities ($n_e \sim 10^{12} \text{ cm}^{-3}$) from spectral lines formed at higher temperatures than O VII. However, due to the lower spectral resolution of the RGS (compared to *Chandra* HETGS), we could not confirm such coronal densities.

In conclusion, this study has confirmed that the abundance ratio pattern in σ^2 CrB's coronae does not follow that of a simple inverse FIP effect or of a solar-like FIP effect, but appears to be more complex. However, the lack of data on photospheric abundances in σ^2 CrB to compare with still casts doubt on whether such a pattern is real or mirrors the stellar composition. Nevertheless, the underabundance of Fe in σ^2 CrB's coronae (compared to the solar photospheric Fe abundance) appears robust and is consistent with its abundance found in the stellar photosphere.

Dr. Rachel Osten is warmly thanked for providing the

Chandra data and model and access to her software, and for useful comments that improved the content of this paper. The Columbia group acknowledges support from NASA to Columbia University for *XMM-Newton* mission support and data analysis. MG acknowledges support from the Swiss National Science Foundation (grant 20-66875.01). Based on observations obtained with *XMM-Newton*, an ESA science mission with instruments and contributions directly funded by ESA Member States and the USA (NASA). We thank an anonymous referee for useful comments that improved this paper.

REFERENCES

- Agrawal, P. C., Markert, T. H., & Riegler, G. R. 1985, *MNRAS*, 213, 761
- Agrawal, P. C., Rao, A. R., & Riegler, G. R. 1986, *MNRAS*, 219, 777
- Agrawal, P. C., White, N. E., & Riegler, G. R. 1981, *MNRAS*, 196, 73P
- Antunes, A., Nagase, F., & White, N. E. 1994, *ApJ*, 436, L83
- Arge, C. N., & Mullan, D. J. 1998 *Sol. Phys.*, 182, 293
- Arnaud, K. A. 1996, in *ASP Conf. Ser. 101, Astronomical Data Analysis Software and Systems V*, ed. G. H. Jacoby & J. Barnes (San Francisco: ASP), 1
- Audard, M., Behar, E., Güdel, M., Raassen, A. J. J., Porquet, E., Mewe, R., Foley, C. R., & Bromage, G. E. 2001b, *A&A*, 365, L329
- Audard, M., Güdel, M., & Mewe, R. 2001a, *A&A*, 365, L318
- Audard, M., Güdel, M., Sres, A., Raassen, A. K. K., & Mewe, R. 2003, *A&A*, 398, 1137
- Audard, M., Telleschi, A., Güdel, M., Skinner, S. L., Pallavicini, R., & Mitra-Kraev, U. 2004, *ApJ*, 617, 531
- Bhatia, A. K. & Doschek, G. A. 1992, *Atomic Data and Nuclear Data Tables*, 52,
- Bakos, G. A. 1984, *AJ*, 89, 1740
- Barden, S. C. 1985, *ApJ*, 295, 162
- Brinkman, A. C., et al. 2001, *A&A*, 365, L324
- Brown, G. V., Beiersdorfer, P., Chen, H., Chen, M. H., & Reed, K. J. 2001, *ApJ*, 557, L75
- Brown, G. V., Beiersdorfer, P., Liedahl, D. A., Wildmann, K., & Kahn, S. M. 1998, *ApJ*, 502, 1015
- Chen, G. X., & Pradhan, A. K. 2002, *Physical Review Letters*, 89, 013202
- Chen, G., Pradhan, A. K., & Eissner, W. 2003, *Journal of Physics B Atomic Molecular Physics*, 36, 453
- Craig, I. J. D. & Brown, J. C. 1976a, *A&A*, 49, 239
- 1976b, *Nature*, 264, 340
- den Herder, J. W., et al. 2001, *A&A*, 365, L7
- Drake, J. J., Brickhouse, N. S., Kashyap, V., Laming, J. M., Huenemoerder, D. P., Smith, R., & Wargelin, B. J. 2001, *ApJ*, 548, L81
- Drake, J. J., Laming, J. M., & Widing, K. G. 1995, *ApJ*, 443, 393
- 1997, *ApJ*, 478, 403
- Drake, S. A., Simon, T., Linsky, K. 1989, *ApJS*, 71, 905
- Feldman, U. 1992, *Physica Scripta Volume T*, 46, 202
- Fourmier, K. B., & Hansen, S. B. 2005, *Phys. Rev. A*, 71, 012717
- Garcia-Alvarez, D., Drake, J. J., Lin, L., Kashyap, V. L., & Ball, B. 2005, 621, 1009
- Grevesse, N., & Sauval, A. J. 1998, *Space Sci. Rev.*, 85, 161
- Güdel, M., et al. 2001a, *A&A*, 365, L336
- Güdel, M., Audard, M., Magee, H., Franciosini, E., Grosso, N., Cordova, F. A., Pallavicini, R., & Mewe, R. 2001b, *A&A*, 365, L344
- Güdel, M., Audard, M., Sres, A., Wehrli, R., Behar, E., Mewe, R., Raassen, A. J. J., & Magee, H. R. M. 2002, *ASP Conf. Ser. 277: Stellar Coronae in the Chandra and XMM-Newton Era*, 497
- Hénoux, J.-C. 1995, *Adv. Space Res.*, 15, 23
- Hénoux, J.-C. 1998, *Space Sci. Rev.*, 85, 215
- Huenemoerder, D. P., Canizares, C. R., Drake, J. J., & Sanz-Forcada, J. 2003, *ApJ*, 595, 1131
- Huenemoerder, D. P., Canizares, C. R., & Schulz, N. S. 2001, *ApJ*, 559, 1135
- Jansen, F., et al. 2001, *A&A*, 365, L1
- Laming, J. M. *ApJ*, 614, 1063
- Laming, J. M. & Drake, J. J. 1999, *ApJ*, 516, 324
- Laming, J. M., Drake, J. J., & Widing, K. G. 1995, *ApJ*, 443, 416
- Laming, J. M., Kink, I., Takacs, E., et al. 2000, *ApJ*, 545, L161
- Lee, J. C., Ogle, P. M., Canizares, C. R., Marshall, H. L., Schulz, N. S., Morales, R., Fabian, A. C., & Iwasawa, K. 2001, *ApJ*, 554, L13
- Lepson, J. K., Beiersdorfer, P., Behar, E., & Kahn, S. M. 2003, *ApJ*, 590, 604
- Lumb, D. H., Gondoin, Ph., & Turner, M. J. L. 2000, *SPIE*, 4140, L22
- McKenzie, J. F. 2000, *Sol. Phys.*, 196, 329
- Meyer, J. P. 1985, *ApJS*, 57, 173
- Morrison, R., & McCammon, D. 1983, *ApJ*, 270, 119
- Ness, J.-U., Schmitt, J. H. M. M., Audard, M., Güdel, M., & Mewe, R. 2003, *A&A*, 407, 347
- Osten, R. A., Brown, A., Ayres, T. R., Linsky, J. L., Drave, S. A., Gagné, M., & Stern, R. A. 2000, *ApJ*, 544, 953
- Osten, R. A., Ayres, T. R., Brown, A., Linsky, J., & Krishnamurthi, A. 2003, *ApJ*, 582, 1073
- Pasquini, L., Schmitt, J. H. M. M., & Pallavicini, R. 1989, *A&A*, 226, 225
- Perryman, M. A. C., et al. 1997, *A&A*, 33, L49
- Porquet, D., Mewe, R., Dubau, J., Raassen, A. J. J., Kaastra, J. S. 2001, *A&A*, 376, 1113
- Raassen, A. J. J., et al. 2002, *A&A*, 389, 228
- Raassen, A. J. J., Mewe, R., Audard, M., & Güdel, M. 2003, *A&A*, 411, 509
- Sako, M., et al. 2003, *ApJ*, 596, 114
- Sanz-Forcada, J., Brickhouse, N. S., & Dupree, A. K. 2003b, *ApJS*, 145, 147
- Sanz-Forcada, J., Favata, F., & Micela, G. 2004, *A&A*, 416, 281
- Sanz-Forcada, J., Maggio, A., & Micela, G. 2003a, *A&A*, 408, 1087
- Schmitt, J. H. M. M., Stern, R. A., Drake, J. J., & Kuerster, M. 1996, *ApJ*, 464, 898
- Schwadron, N. A., Fisk, L. A., & Zurbuchen, T. H. 1999, *ApJ*, 521, 859
- Smith, R. K., Brickhouse, N. S., Liedahl, D. A., & Raymond, J. C. 2001, *ApJ*, 556, L91
- Stern, R. A., Uchida, Y., Walter, F., Vilhu, O., Hannikainen, D., Brown, A., Veale, A., & Haisch, B. M. 1992, *ApJ*, 391, 760
- Strassmeier, K. G., Hall, D. S., Fekel, F. C., & Scheck, M. 1993, *A&AS*, 100, 173
- Strassmeier, K. G., Rice, J. B. 2003, *A&A*, 399, 315
- Telleschi, A., Güdel, M., Briggs, K. R., Audard, M., Ness, J.-U., & Skinner, S. L. 2004, *ApJ*, 622, 653
- Testa, P., Drake, J. J., Peres, G. 2004, *ApJ*, 617, 508
- Turner, M. J. L., et al. 2001, *A&A*, 365, L27
- van den Besselaar, E. J. M., Raassen, A. J. J., Mewe, R., van der Meer, R. L. J., Güdel, M., & Audard, M. 2003, *A&A*, 411, 587
- den Oord, G. H. J., Mewe, R., & Brinkman, A. C. 1988, *A&A*, 205, 181
- White, N. E., et al. 1994, *PASJ*, 46, L97

TABLE 1
OBSERVATION LOG.

Instrument	Mode	Filter	Observation Start (UT)	Observation End (UT)	Total Exposure (ks)	Filtered Exposure ^a (ks)
REVOLUTION 316, OBSERVATION ID 0111470201 (“201”)						
RGS1	Spectroscopy	None	2001 Aug 31 07:38:02	2001 Aug 31 13:02:20	19.5	18.9
RGS2	Spectroscopy	None	2001 Aug 31 07:38:02	2001 Aug 31 13:05:11	19.6	18.5
MOS1 ^b . . .	TIMING	Thick	2001 Aug 31 07:44:30	2001 Aug 31 11:32:36	13.7	...
MOS2	IMAGING	Medium	2001 Aug 31 07:44:33	2001 Aug 31 11:34:12	13.8	9.8
PN	TIMING	Medium	2001 Aug 31 08:13:58	2001 Aug 31 13:08:00	17.6	...
REVOLUTION 404, OBSERVATION ID 0111470301 (“301”)						
RGS1	Spectroscopy	None	2002 Feb 22 23:23:29	2002 Feb 23 05:47:04	23.0	22.5
RGS2	Spectroscopy	None	2002 Feb 22 23:23:29	2002 Feb 23 05:47:05	23.0	21.8
MOS1 ^b . . .	TIMING	Thick	2002 Feb 22 23:29:57	2002 Feb 23 05:27:24	21.4	...
MOS2	IMAGING	Medium	2002 Feb 22 23:29:59	2002 Feb 23 05:27:53	21.5	6.7
PN ^b	TIMING	Medium	2002 Feb 22 23:59:25	2002 Feb 23 05:46:27	20.8	...

NOTE. — Data from Revolution 315 are not included for analysis due to short exposure times of approximately 7ks and significant background contamination from solar flare activity.

^aMaximum effective integration time used for data analysis.

^bThe EPIC MOS1 and pn data were not used in this paper.

TABLE 2
 WAVELENGTH RANGES
 EXCLUDED FROM THE
 FITTING PROCEDURE.

Instrument	λ Range (\AA)
RGS	≤ 8.3
RGS	15.80-16.20
RGS	18.60-18.80
RGS	19.50-19.90
RGS	20.00-20.30
RGS	20.60-20.80
RGS	21.15-21.30
RGS	21.40-21.50
RGS	23.40-23.70
RGS	24.10-24.60
RGS	24.90-25.25
RGS	25.45-25.80
RGS	26.25-26.50
RGS	27.00-27.20
RGS	27.30-27.70
RGS	27.80-28.10
RGS	28.30-28.50
RGS	29.40-29.70
RGS	30.20-30.60
RGS	30.90-31.15
RGS	31.50-31.70
RGS	32.10-33.55
RGS	33.85-34.00
RGS	34.50-34.65
RGS	35.60-35.80
RGS	36.30-36.85
RGS	37.50-37.80
MOS2	≤ 1.65
MOS2	≥ 18

TABLE 3
 BEST-FIT PARAMETERS FOR RGS+MOS2 TOGETHER WITH
 ABUNDANCES FROM OSTEN ET AL. (2003).

Parameters	201	301	Osten et al. (2003)
[C/Fe]	$-0.24^{+0.05}_{-0.10}$	$-0.28^{+0.08}_{-0.09}$...
[N/Fe]	$-0.09^{+0.08}_{-0.11}$	$-0.16^{+0.10}_{-0.10}$	$-0.07^{+0.07}_{-0.08}$
[O/Fe]	$-0.22^{+0.02}_{-0.04}$	$-0.22^{+0.03}_{-0.05}$	$-0.16^{+0.01}_{-0.01}$
[Ne/Fe]	$+0.11^{+0.04}_{-0.03}$	$+0.15^{+0.05}_{-0.05}$	$+0.16^{+0.01}_{-0.01}$
[Mg/Fe]	$+0.04^{+0.04}_{-0.04}$	$+0.08^{+0.05}_{-0.05}$	$-0.00^{+0.01}_{-0.01}$
[Si/Fe]	$-0.06^{+0.04}_{-0.07}$	$-0.09^{+0.08}_{-0.09}$	$-0.10^{+0.01}_{-0.01}$
[S/Fe]	$-0.45^{+0.13}_{-0.19}$	$-0.49^{+0.19}_{-0.32}$	$-0.28^{+0.05}_{-0.05}$
[Ar/Fe]	$+0.04^{+0.29}_{-0.35}$	$-0.35^{+0.32}_{-\infty}$	$+0.34^{+0.11}_{-0.14}$
[Ca/Fe]	$-0.12^{+0.30}_{-\infty}$	$+0.16^{+0.25}_{-0.53}$...
[Fe/H]	$-0.17^{+0.01}_{-0.01}$	$-0.13^{+0.02}_{-0.02}$	$-0.34^{+0.02}_{-0.02}$
T_1 (MK)	$3.83^{+0.10}_{-0.26}$	$3.34^{+0.18}_{-0.19}$...
T_2 (MK)	$7.74^{+0.08}_{-0.08}$	$7.48^{+0.08}_{-0.08}$...
T_3 (MK)	$14.7^{+0.56}_{-0.52}$	$14.4^{+0.50}_{-0.60}$...
T_4 (MK)	$28.4^{+8.19}_{-0.13}$	$31.6^{+5.00}_{-3.40}$...
$\log EM_1$ (cm ⁻³)	$52.7^{+0.10}_{-0.10}$	$52.5^{+0.10}_{-0.10}$...
$\log EM_2$ (cm ⁻³)	$53.1^{+0.10}_{-0.10}$	$53.1^{+0.10}_{-0.10}$...
$\log EM_3$ (cm ⁻³)	$52.9^{+0.10}_{-0.10}$	$52.9^{+0.10}_{-0.10}$...
$\log EM_4$ (cm ⁻³)	$52.7^{+0.10}_{-0.10}$	$52.8^{+0.10}_{-0.10}$...
χ^2	1.34	1.48	

TABLE 4
PHOTON FLUXES FOR O VII
TRIPLET AND Fe XVII LINES.

Wavelength (Å)	Flux (10^{-4} ph cm $^{-2}$ s $^{-1}$)
21.60	3.65 ± 0.28
21.80	0.80 ± 0.20
22.10	2.25 ± 0.25
15.01	13.9 ± 0.30
15.26	4.60 ± 0.21

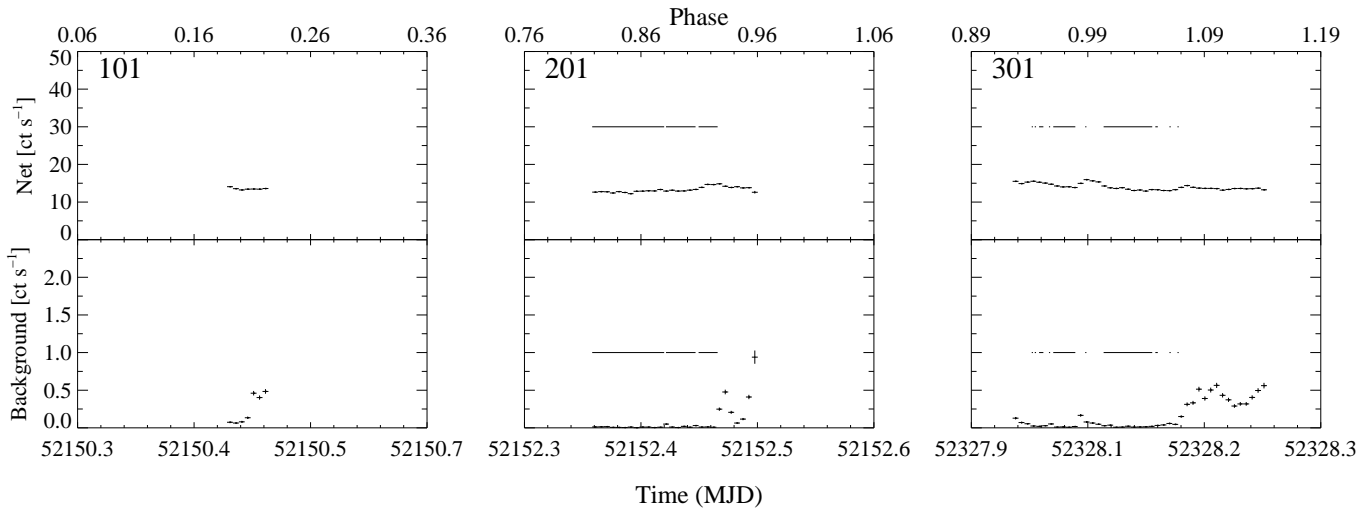


FIG. 1.— EPIC MOS2 lightcurves with a bin size of 500 s for the three observation dates (error bars are shown). The selected good time intervals are shown by horizontal lines above the lightcurves. The excluded time ranges are during high background solar flare activities. The net count rates are reasonably constant.

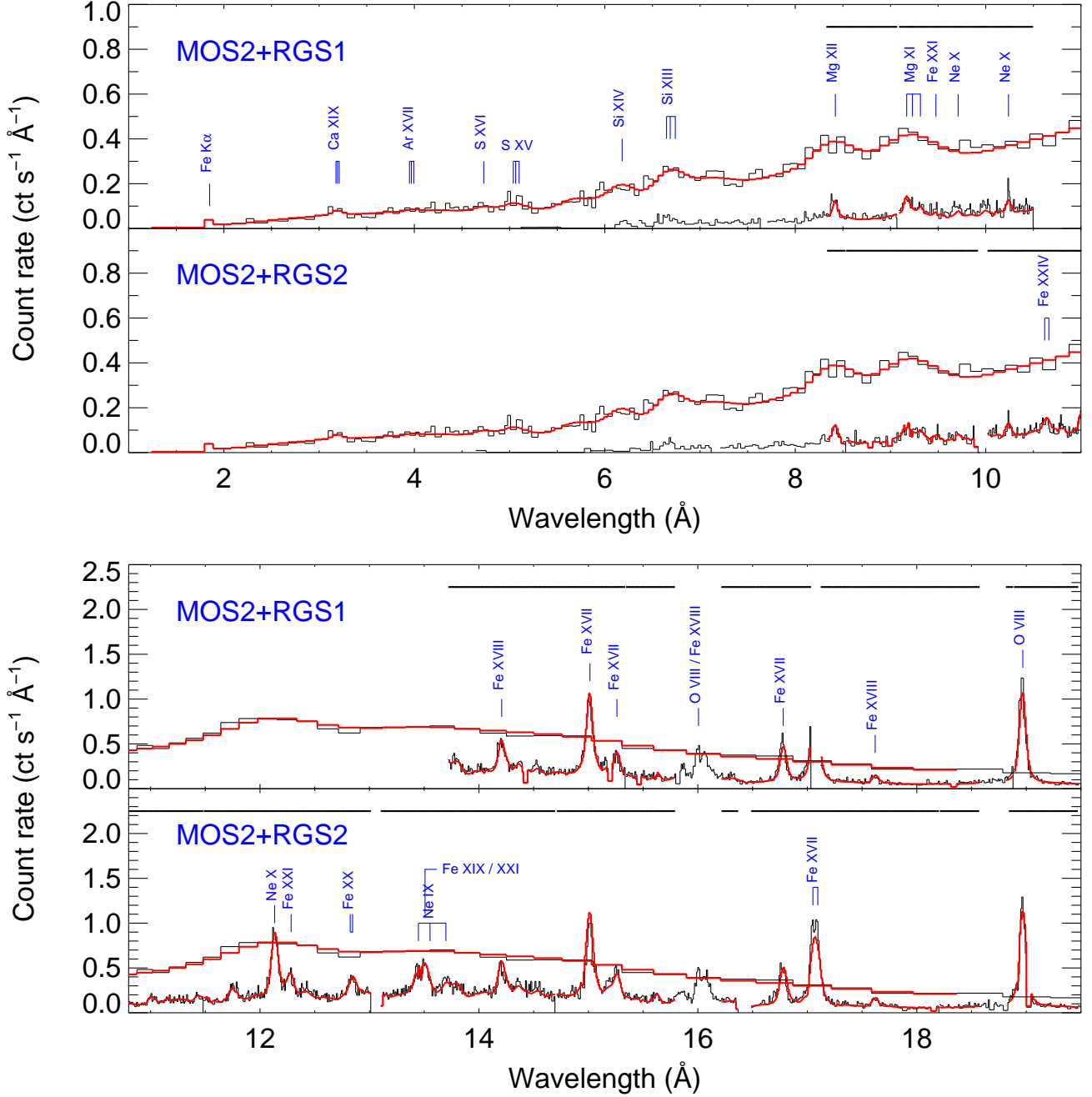


FIG. 2A.— (a) *XMM-Newton* MOS2, RGS1, and RGS2 spectra with the EPIC MOS2+RGS (301; see Tab. 3) best-fit model (superposed line) for 1–20 Å. Error bars are not shown for clarity. The model is only shown in the wavelength ranges used for the spectral fits (see Tab. 2). The ranges for the RGS are also shown at the top of each panel as broken lines. (b) Same as (a), but for 20–40 Å.

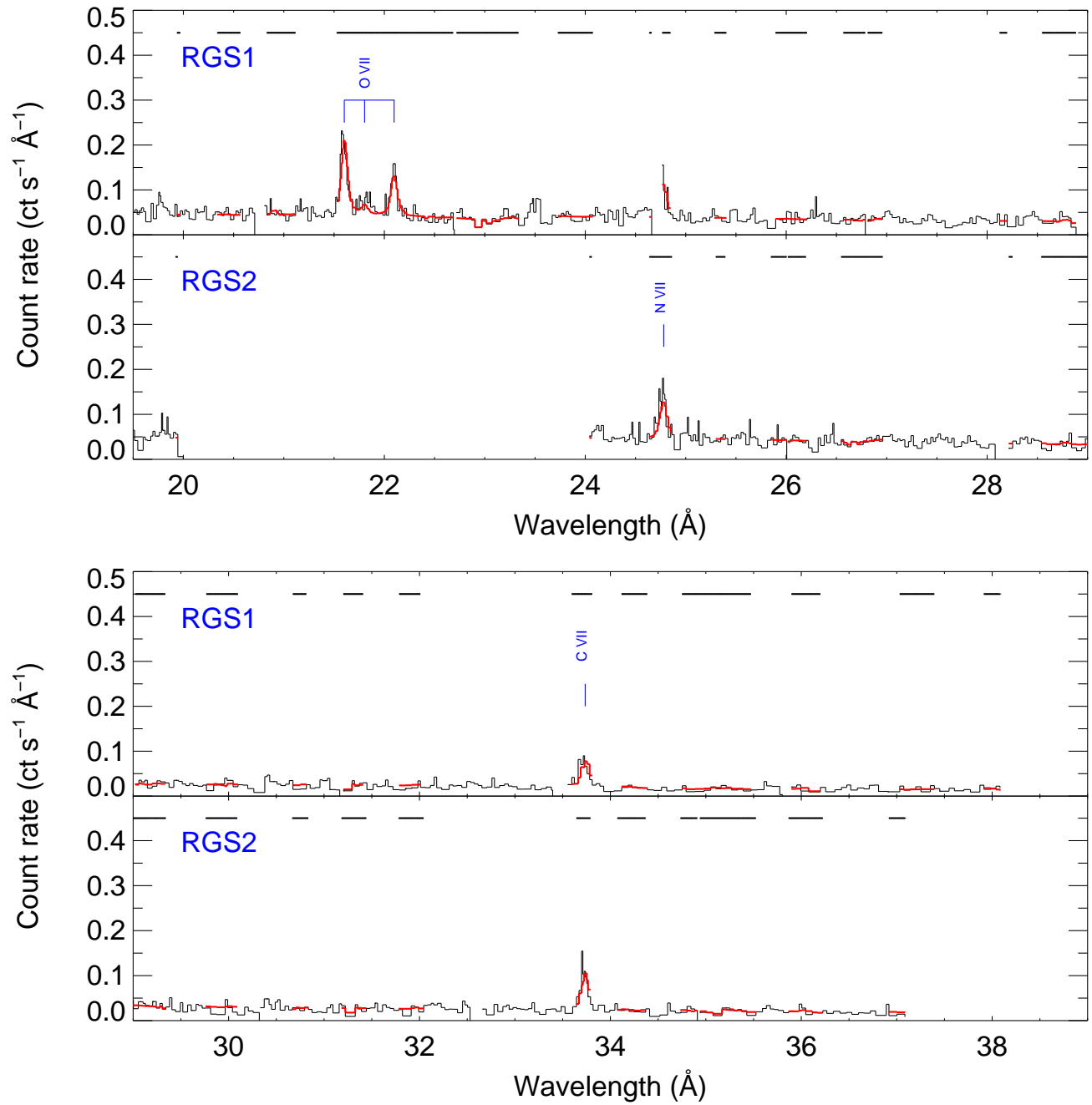


FIG. 2B.—

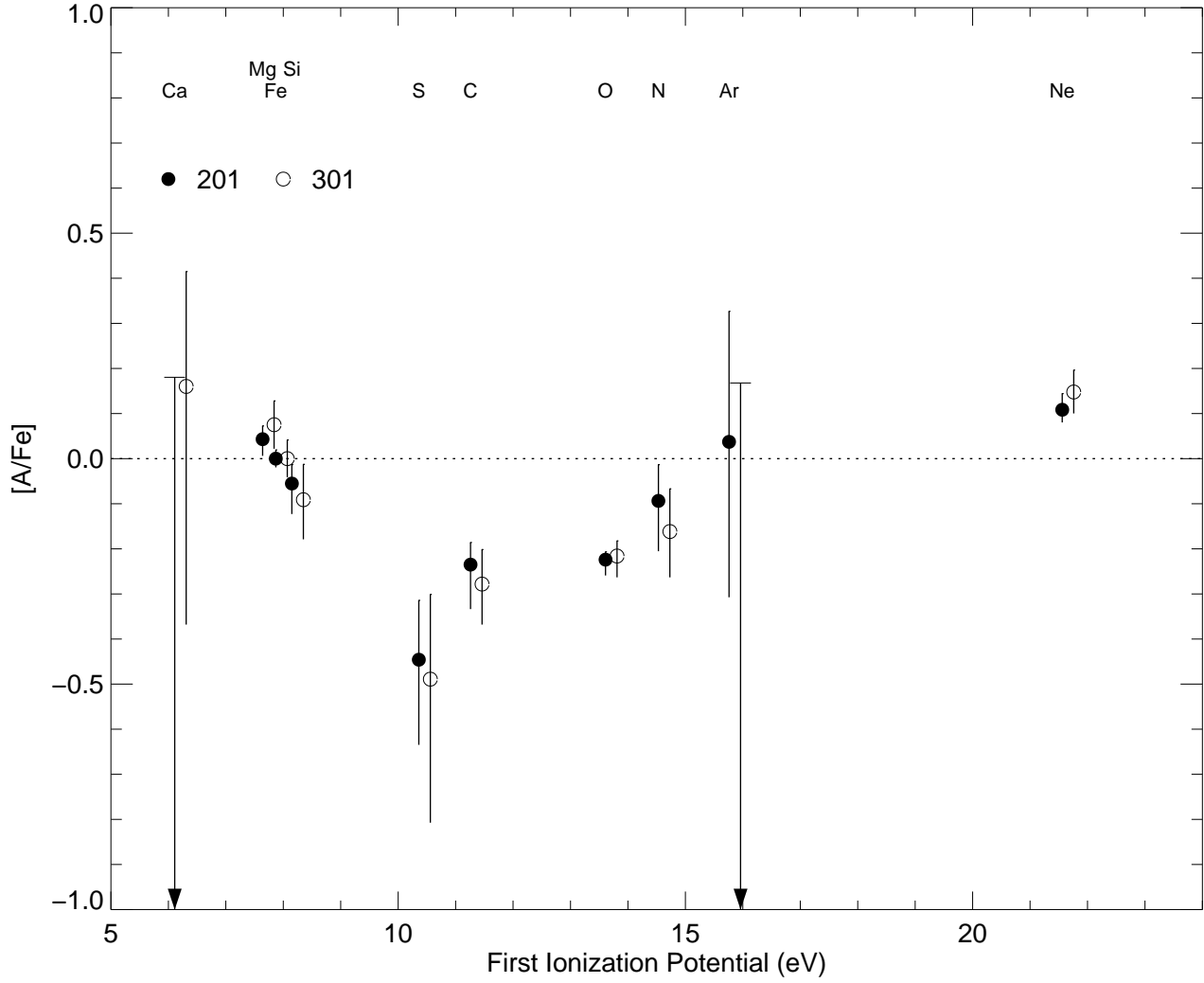


FIG. 3.— Abundance ratios relative to Fe and relative to solar abundances (Grevesse & Sauval 1998) for the 201 and 301 observations as a function of the FIP. For clarity, we shifted the 301 data points by +0.2 eV. Statistical errors only are shown; systematic errors probably range up to 0.1–0.2 dex. For Ca (201) and Ar (301), upper limits are shown with an arrow down to the bottom of the figure.

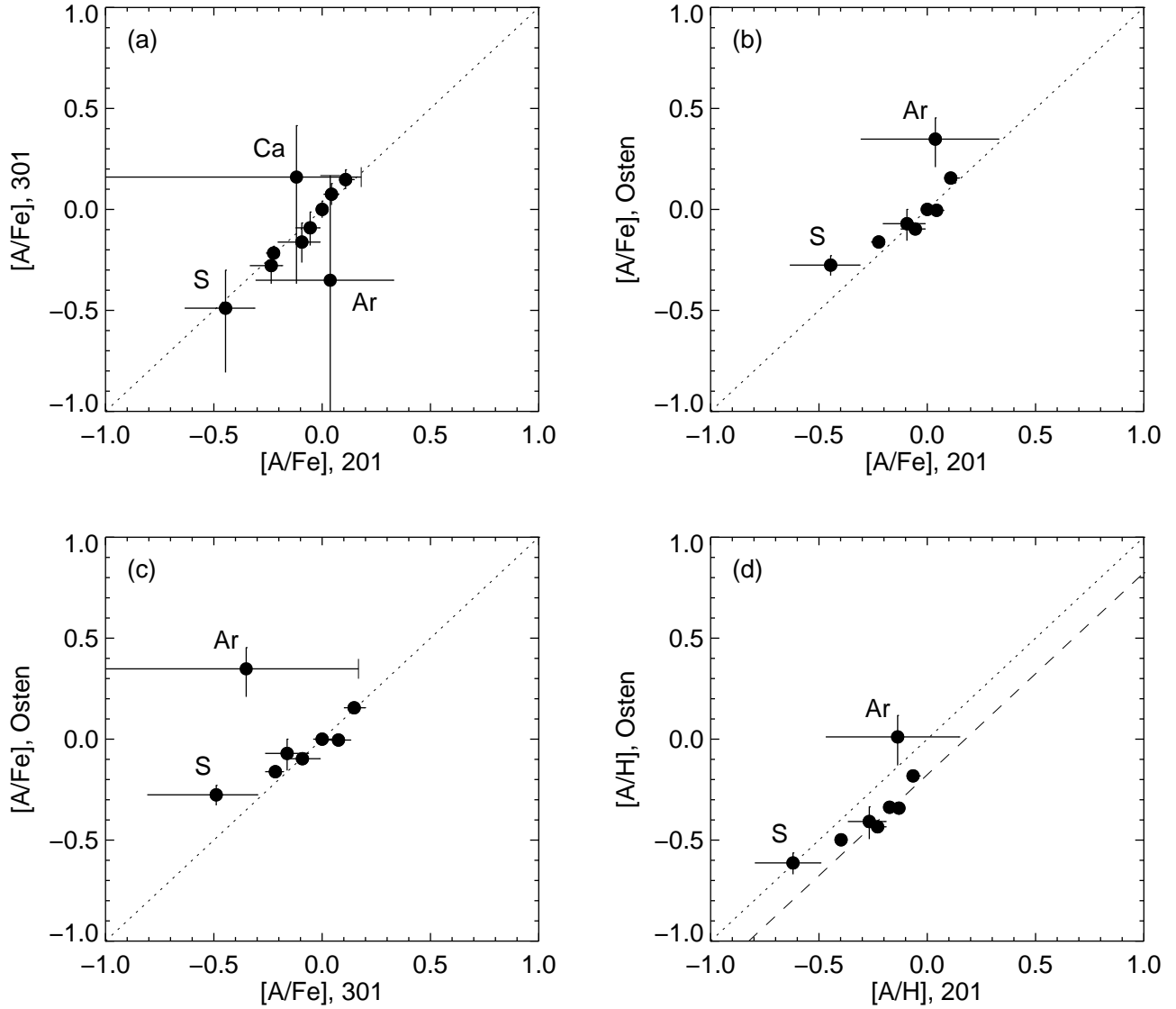


FIG. 4.— Comparisons between abundances obtained in this paper and with those by Osten et al. (2003). The bottom right panel (d) shows absolute abundances instead of abundance ratios to Fe (a,b,c). Abundance ratios are robust and similar, whereas our absolute (relative to H) abundances are systematically higher than those derived by Osten et al. (2003). Some abundances discussed in the text are labeled for clarity. The dotted line represents a 1:1 correlation, whereas the dashed line in panel d represents a 1.5:1 correlation.

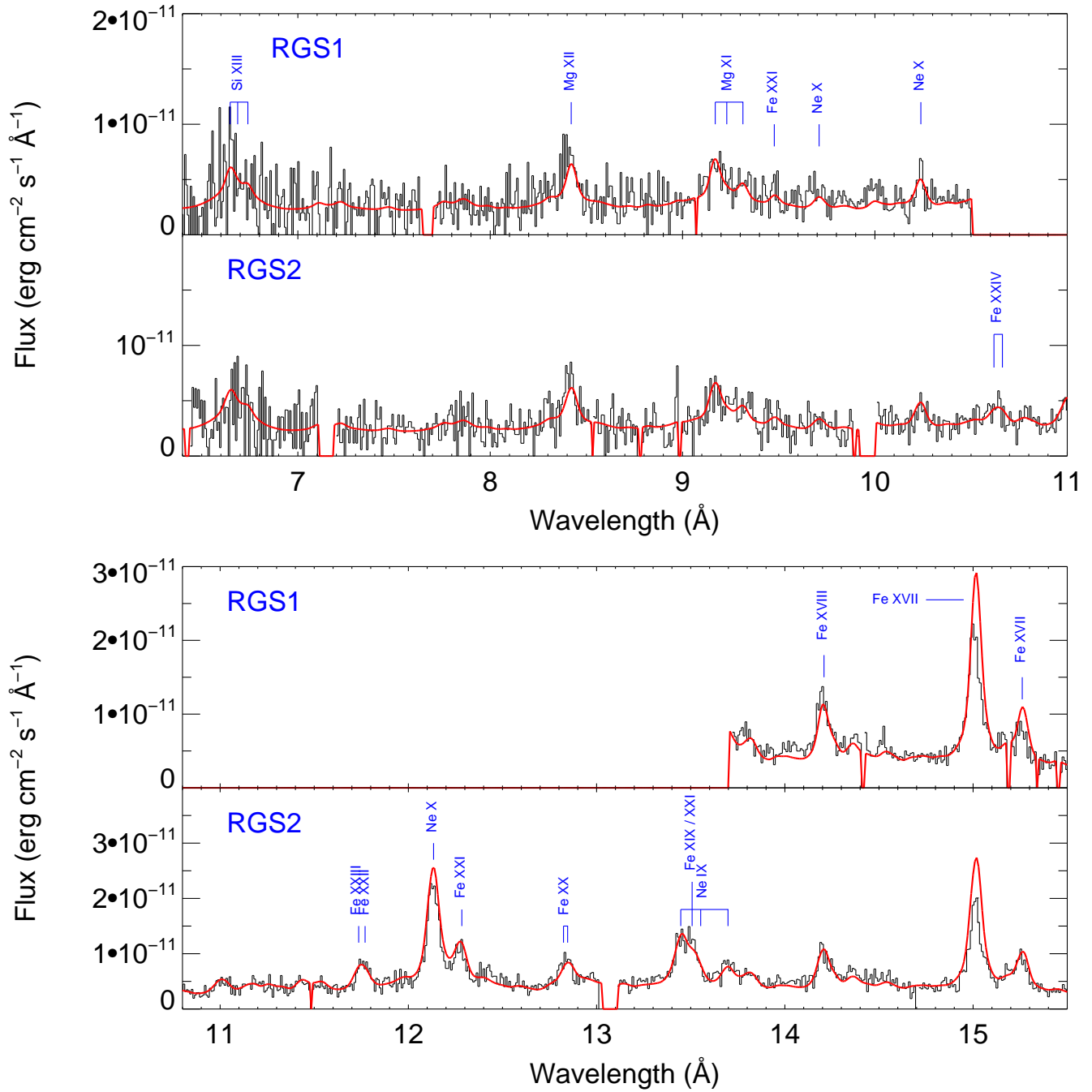


FIG. 5A.— (a) *XMM-Newton* RGS1 and RGS2 fluxed spectra (uncorrected for interstellar absorption which is in any case negligible in this wavelength range) compared with the *Chandra* quiescent model (superposed line) of Osten et al. (2003) for 6.5–15.5 \AA . Error bars are not shown for clarity. (b) Same as (a), but for 15–25 \AA . (c) Same as (a) but for 25–35 \AA .

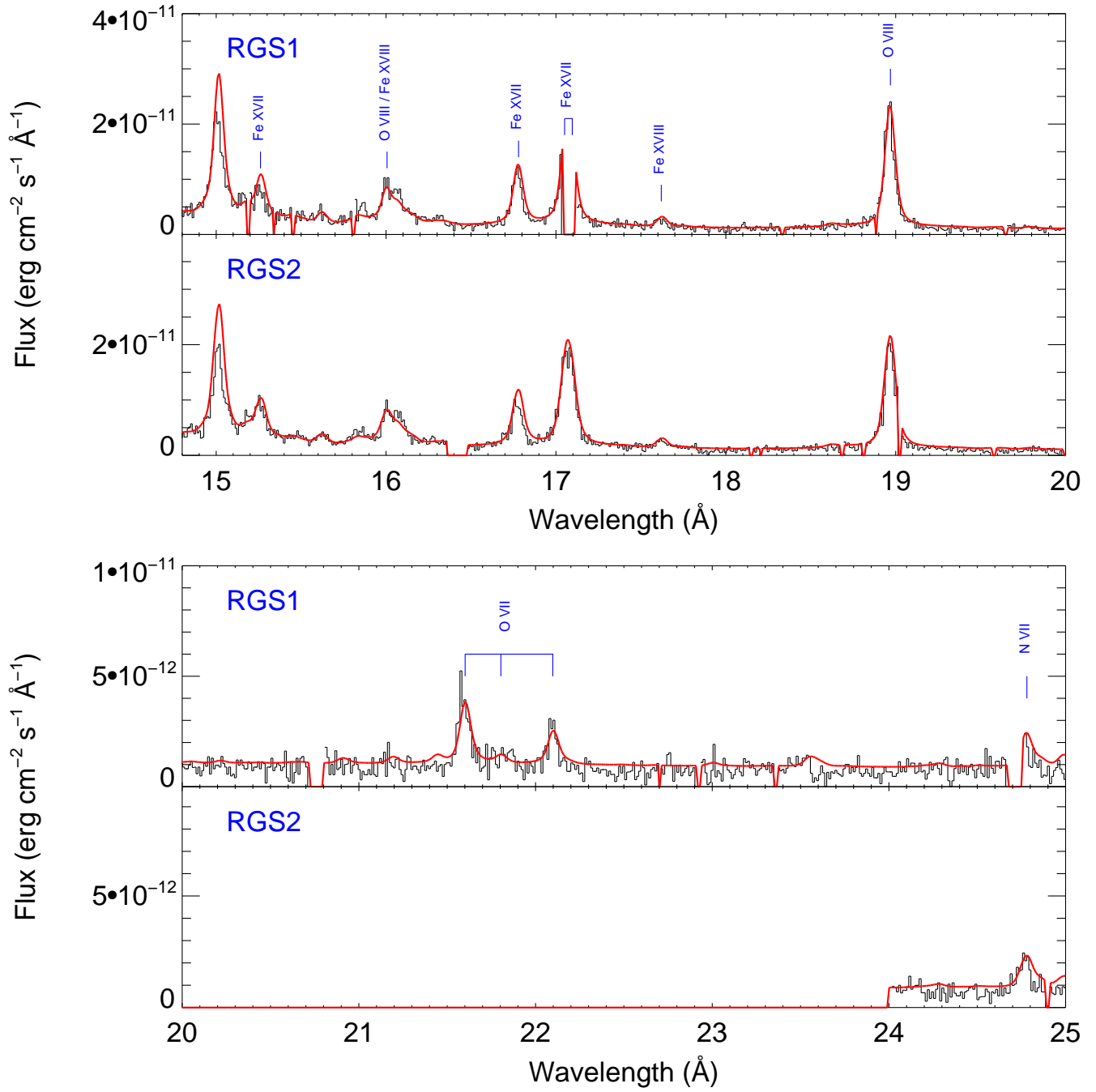


FIG. 5B.—

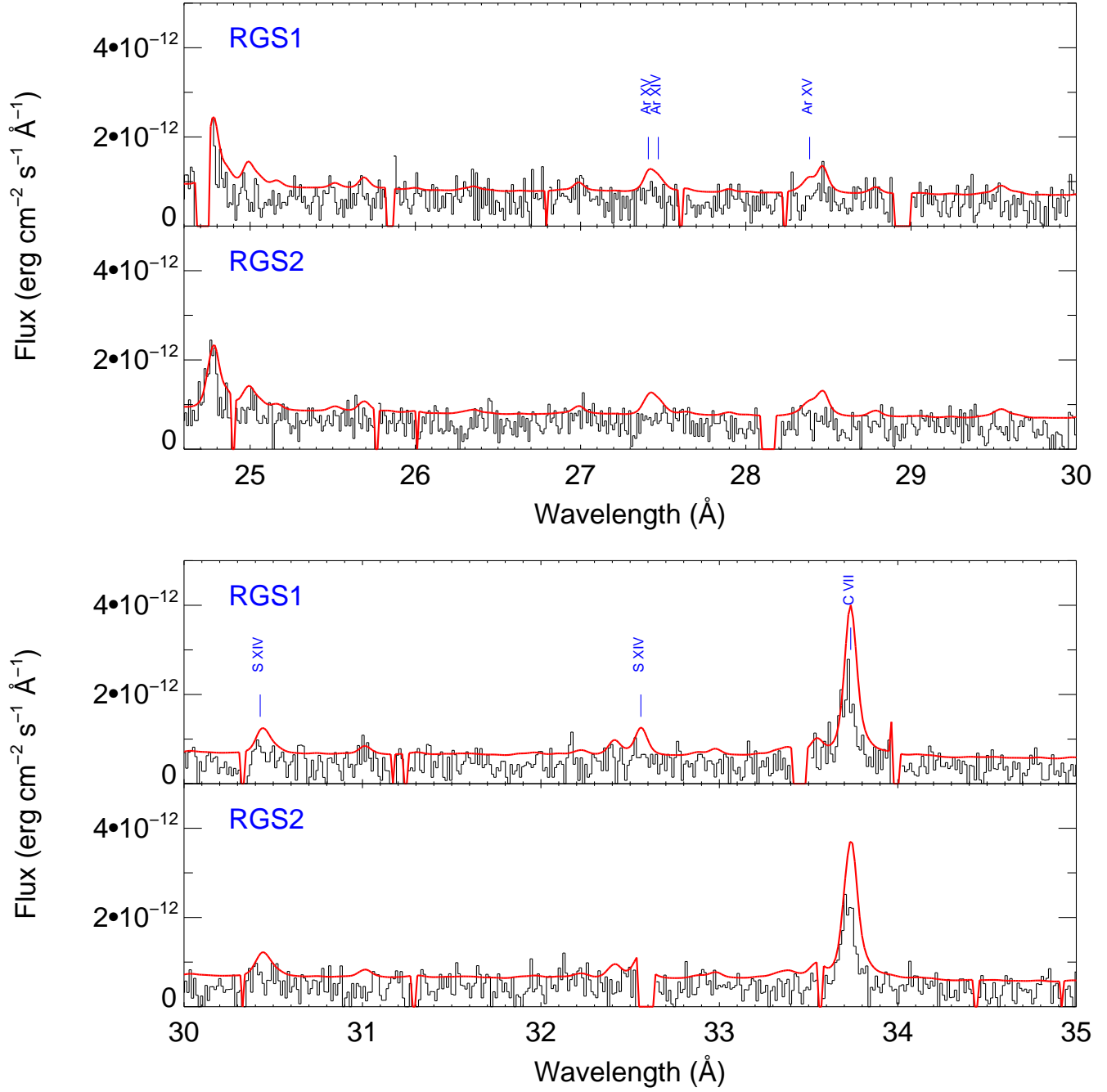


FIG. 5C.—

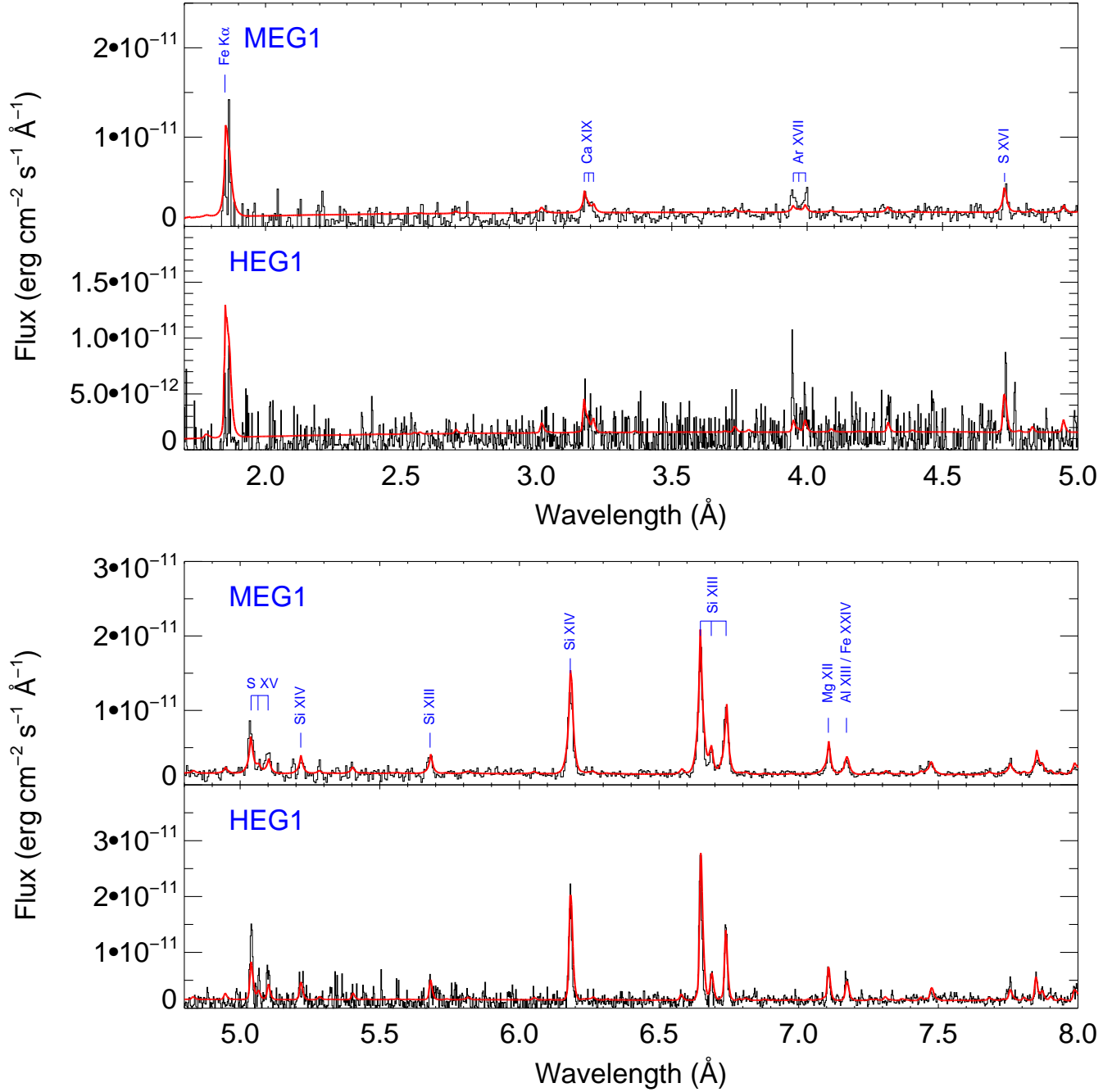


FIG. 6A.— (a) *Chandra* MEG1 and HEG1 fluxed spectra (uncorrected for interstellar absorption which is in any case negligible in this wavelength range) compared with our *XMM-Newton* EPIC MOS2+RGS (301) best-fit model (superposed line). (b) Same as (a), but for 8–14 Å. (c) Same as (a) but for 14–26 Å. The 17–26 Å panels show the MEG data only.

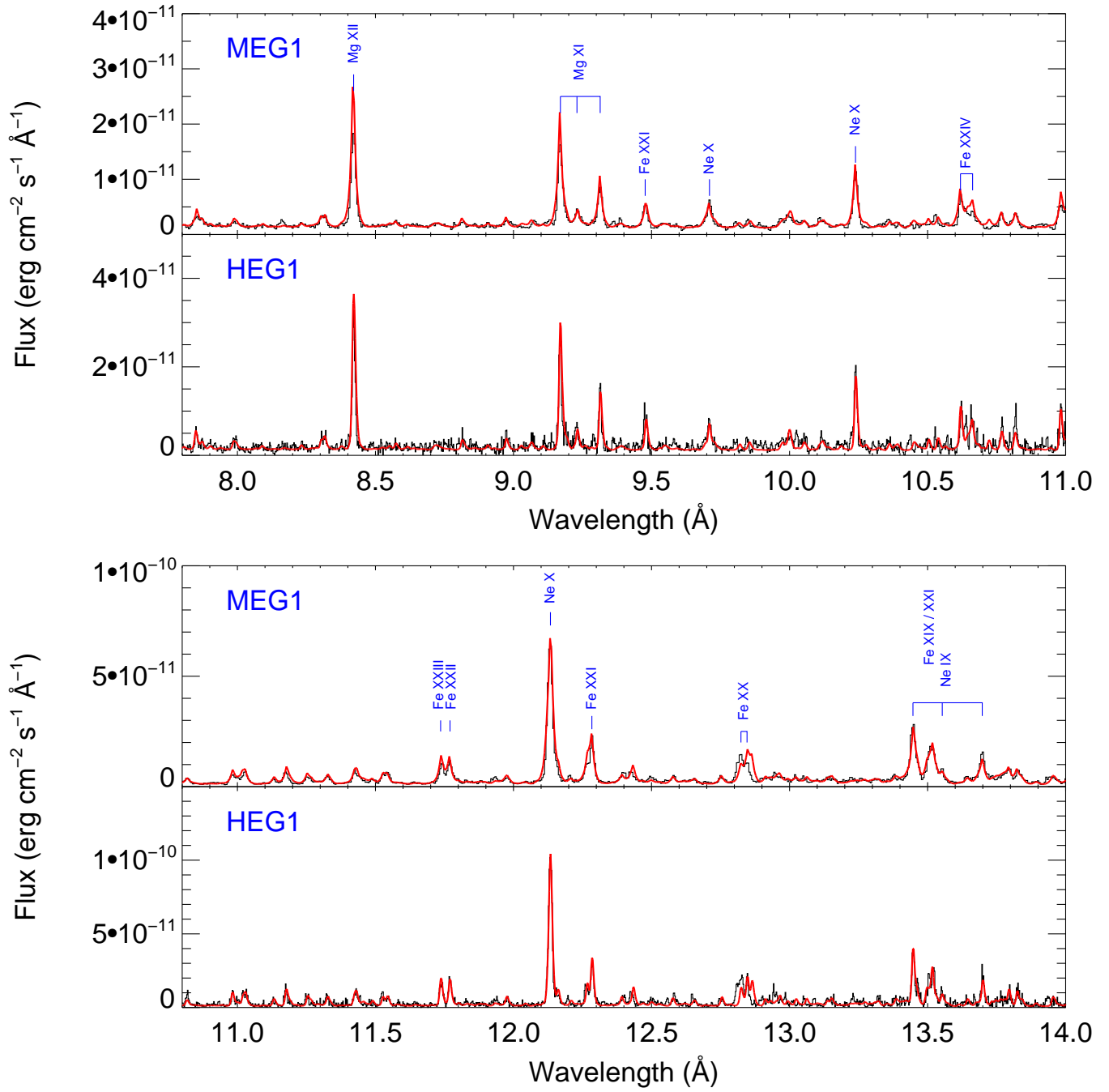


FIG. 6B.—

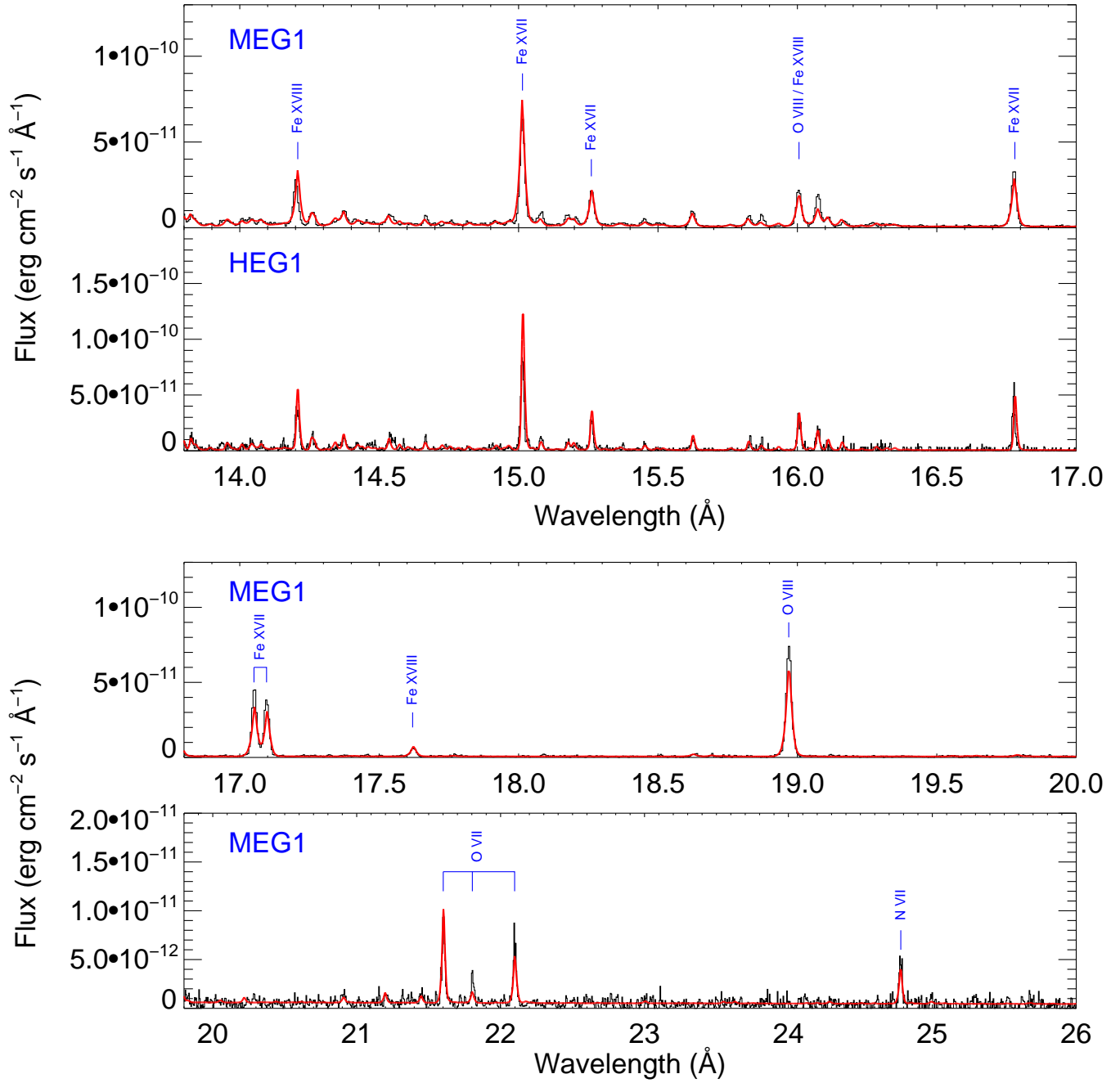


FIG. 6C.—